Applied Mathematical Modelling 130 (2024) 693–712

Contents lists available at ScienceDirect

Applied Mathematical Modelling

journal homepage: www.elsevier.com/locate/apm

Accelerated process parameter selection of polymer-based selective laser sintering via hybrid physics-informed neural network and finite element surrogate modelling

Hao-Ping Yeh [a,*], Mohamad Bayat [a], Amirhossein Arzani [b,c], Jesper H. Hattel [a]

[a] Department of Civil and Mechanical Engineering, Technical University of Denmark, Building 425, 2800 Kgs. Lyngby, Denmark
[b] Scientific Computing and Imaging Institute, University of Utah, WEB Building, Salt Lake City, UT 84112, USA
[c] Department of Mechanical Engineering, University of Utah, MEK Building, Salt Lake City, UT 84112, USA

ARTICLE INFO

Keywords:
Physics-informed neural network
Thermal analysis
Melt pool
Selective laser sintering
Polymer

ABSTRACT

The state of the melt region as well as the temperature field are critical indicators reflecting the stability of the process and subsequent product quality in selective laser sintering (SLS). The present study compares various simulation models for analyzing melt pool morphologies, specifically considering their complex transient evolution. While thermal fluid dynamic simulations offer comprehensive insights into melt regions, their inherent high computational time demand is a drawback. In SLS, the polymer's high viscosity and low conductivity limit liquid flow, thereby promoting a slow evolution of the melt region formation. Based on this observation, utilizing low-complexity pure heat conduction simulation can be adequate for describing melt region morphologies as compared to the more complex thermal fluid dynamic simulations. In the present work, we propose such a purely conduction based finite element (FE) model and use it in combination with an AI-powered partial differential equation (PDE) solver based on a parametric physics-informed neural network (PINN). We specifically conduct the simulations for the sintering process, where large thermal gradients are present, with the parametric PINN based model, whereas we employ the finite element method (FEM) for the cooling phase in which gradients and cooling rates are several orders lower, thus enabling the prediction of sintering temperature and melt region morphology under various configurations. The combined hybrid model demonstrates less than 7% deviation in temperatures and less than 1% in melt pool sizes as compared to the pure FEM-based models, with faster computational times of 0.7 s for sintering and 20 min for cooling. Moreover, the hybrid model is utilized for multi-track simulation with parametric variations with the purpose of optimizing the manufacturing process. Our model provides an approach to determine the most suitable combinations of settings that enhance manufacturing speed while preventing issues such as lack of fusion and material degradation.

1. Introduction

Selective laser sintering (SLS) is a form of laser powder bed fusion (L-PBF) additive manufacturing (AM) technology that fabricates three-dimensional objects layer by layer [1]; see Fig. 1 (a). The procedure begins with preparing a powder bed with a fine layer of

---

[*] Corresponding author.
E-mail address: haoye@dtu.dk (H.-P. Yeh).

https://doi.org/10.1016/j.apm.2024.03.030
Received 29 January 2024; Received in revised form 19 March 2024; Accepted 27 March 2024

particles uniformly spread across the 3D printer's build platform. Subsequently, the laser scans the intended cross-section of the object, as specified in the CAD file. Upon encountering the material, the laser heats and selectively fuses the particles, forming a solid layer. This cycle of applying powder layers and scanning with the laser is continued until the entire part is completed. Polymer-based SLS can produce strong, complex, and functional parts utilized in consumer goods, prototyping [2], aerospace [3], and healthcare devices [2]. However, despite its advantages, polymer-based SLS can still exhibit certain limitations and defects in the resulting products. Common issues include lack of fusion, porous structures, and high surface roughness [3–5]. The interaction between the laser and the powder bed leads to the formation of a molten region. Inadequate fusion and porosity can especially occur when a low-power laser generates a molten region which is too small.

As opposed to this, material degradation and dimensional inaccuracy can occur when the laser power is too high, leading to overheating [6,7]. Hence, the size and characteristics of the melt region can serve as a crucial indicator for regulating and ensuring the quality of the final products [8]. Typically, two primary approaches are suggested for studying the melt region dimensions, *in-situ* sensing [9] and numerical simulations. Several research studies have focused on using imaging techniques to assess factors such as the melt pool size and temperature and the part's porosity in L-PBF. However, the practical application of *in-situ* sensing is constrained by high costs, complexity, limited spatial resolution, and the need for extensive data management. Multiple researchers have been engaged in simulating the initial powder bed preparation using the discrete element method (DEM) [10–12] followed by employing the finite volume method (FVM)-based thermal fluid dynamic models [13]. They aim to forecast parameters like melt pool dimensions [14,15], the formation of keyholes [16], and the quality including potential porosities of the final surface [17] in metal or polymer L-PBF processes. An inherent characteristic of multiphysics models in simulating product defects and melt pool morphologies in various processes is the significantly long calculation times and this is also the case for SLS of polymers. This is primarily due to the material characteristics of polymers, such as high viscosity, low flowability, and low conductivity, which result in a very slow evolution of the melt region during sintering itself as well as during the subsequent cooling [3,18].

For that reason, there have been several contributions in the literature on pure conductive models of L-PBF of metals [19,20]. Furthermore, there have also been contributions on pure conductive models of L-PBF of polymers. Riedlbauer et al. introduced a finite element (FE) thermal model focused on a single-track approach using PA12 [21]. It investigated the correlation between laser parameters and the melt region's behavior, temperature, and size. The simulation model's precision was validated by comparing its outputs with experimental data and measurements, affirming its accuracy.

Over the past few years, a growing number of researchers have been working on AI-based simulations for L-PBF processes, aiming to decrease simulation time while maintaining accuracy. Based on the amount of data required, there are mainly two types of models, i.e., data-driven and physics-informed models [23]. Regarding data-driven models [24,25], Zhang et al. [26] utilized sensors to gather temperature data from the melt pool while varying relevant process parameters. They employed this collected data as datasets for training two different models: XGBoost and long short-term memory (LSTM). These models were designed to establish mappings between process parameters and their respective temperature values within the melt pool. Ren et al. [27] created a data-driven model predicting the temperature evolution in a single layer produced with different scanning strategies in directed energy deposition (DED). The dataset was based on FEM simulation of 100 different geometries and six distinct scanning strategies. Their model attained a prediction accuracy of 95% with respect to test data from which it was not trained, demonstrating its effectiveness in forecasting the thermal field evolution for different scanning strategies in AM. Data-driven models perform well in LPBF thermal simulations, but their accuracy relies heavily on the dataset size [28], which can be expensive. On the other hand, physics-informed models [29–33] incorporate physics-based knowledge, i.e. partial differential equations (PDEs) into the network architecture, thus requiring minimal or even no extensive datasets [34,35], making them more suitable and practical for industrial applications. Hosseini et al. [36] applied a physics-informed neural network (PINN) to address the parametric 3D transient heat conduction equation for predicting the temperature in L-PBF single-track simulation. The model demonstrated generalizability within specified ranges of laser settings and material properties, and it was verified with results from their own FE model. Similarly, Li et al. [37] also utilized PINN to predict

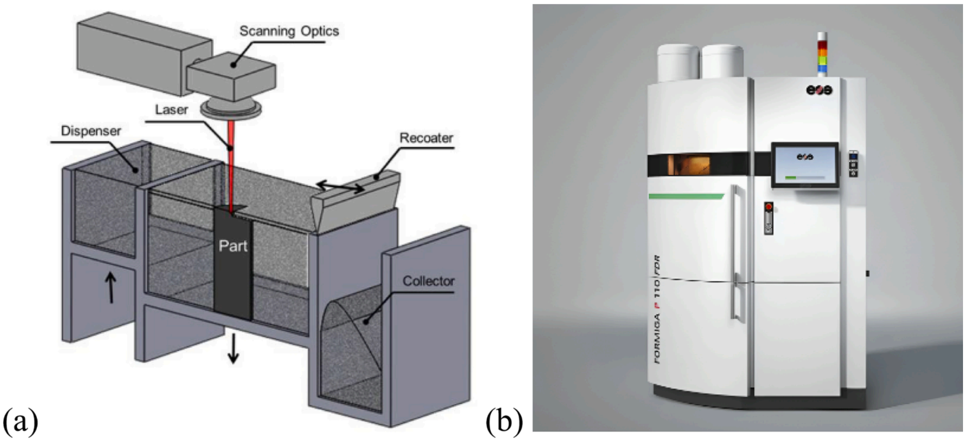

Fig. 1. (a) Schematic of the SLS process [22] (b) The EOS P110 FDR SLS machine, which is used in the present study.

single-track temperature profiles during metal-based L-PBF. In order to adapt the model to various manufacturing parameters efficiently, the transfer learning technique was utilized to save training time. The model achieved an error of less than 2% compared to their own FE model. Lastly, the PINN-based hybrid model mixing partial-domain temperature data and physics-based knowledge was adopted by Liao et al. [38] to predict the full-domain temperature in L-PBF and DED of a metal single-track. Furthermore, the model demonstrated the capability to identify unknown properties of material by solving the inverse problem based on the obtained temperature data from their FE model.

The purpose of the present paper is twofold. First, we present and compare different models of varying complexity ranging from full computational fluid dynamics (CFD) to purely conductive models for the polymer-based SLS process. Thereafter, we create an artificial intelligence (AI)-assisted hybrid surrogate model to accurately and efficiently predict the melt region's transient temperature level and morphologies during manufacturing. This model offers an opportunity for rapid fine-tuning and optimization of process parameters. More specifically, we initially utilize an FVM thermal fluid dynamic simulation as our CFD model, incorporating phase change, heat transfer, Marangoni effect, and liquid flow within the commercial software, Flow-3D. This should strictly speaking be done on a loose powder bed as we did in [39]. Previously, we validated this approach against experimental values for melt region width and depth and found good agreement [39]. However, this numerical procedure on the loose powder bed took around three weeks in computational time on an Intel Xeon w-2195 processor. Hence, in the present work, we do the CFD simulation on a dense substrate effectively reducing calculation time down to four days. This simulation is subsequently validated against in-house experimental results to ensure accuracy [39,40]. Following this, we observe that the inherent low flowability of the polymer restricts the activity of the liquid flow [41], resulting in the liquid convection having limited impact on evolution of the dimensions of the melt region. Consequently, the thermal fluid dynamic model on the dense substrate will be further simplified to a thermal conduction model using the FEM solver FEniCS [42], which proves adequate for describing the melt pool morphologies of SLS of high viscosity polymers.

In the current work, we present a comparative study of four different models ranging from a complex FVM-based thermal fluid dynamic model including a dense powder bed to a much less complex FEM-based thermal conduction model. The basis of our simulations is experiments carried out on the machine (EOS P110FDR (Fig. 1 (b)), where the laser settings (speed and power), and the applied material (PA11) we are working with, results in the formation of a sintering track which becomes apparent during the cooling stage following laser sintering. It is important to note that in the FEM simulation, most of the simulation time consists of the sintering

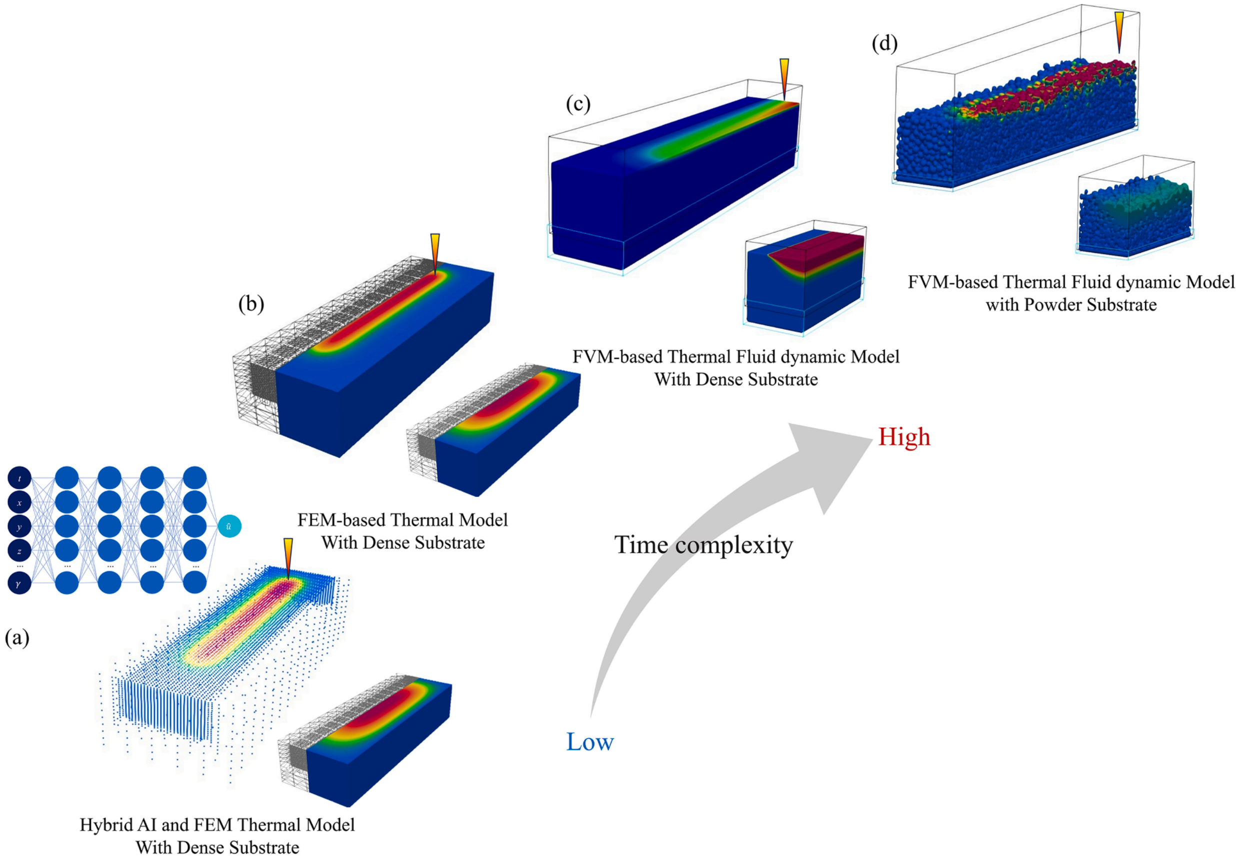

Fig. 2. A comparative analysis of models (a) AI-based heat transfer simulation (b) FEM-based heat transfer simulation (c) FVM-based thermal fluid dynamic simulation with dense substrate (d) FVM-based thermal fluid dynamic simulation with powder substrate, ranging from low to high time complexity.

phase because of the very small-time increments needed to capture the moving heat source accurately. Hence, we develop a hybrid physics-informed machine learning and FEM surrogate model to obtain sintering temperature and melt region morphologies during sintering, as summarized in Fig. 2. First, parametric PINN predicts single-track temperature profiles corresponding to different laser settings during sintering. Second, in the cooling phase, the temperature results predicted by PINN during sintering are utilized as initial conditions for the subsequent FEM-based conduction simulations. Notably, the FEM simulation is chosen over PINN for the cooling phase due to its superior time efficiency in handling the specific initial conditions from sintering, thereby eliminating the need to train distinct PINN models for these conditions. The simulated temperature and melt pool sizes from the hybrid model are verified against the FEM-based heat conduction model, showing less than a 7% and 1% deviation, respectively. The training time for the parametric sintering model is 7 h, using an NVIDIA A100 Tensor Core GPU. The prediction time for sintering has been notably reduced to 0.7 s, with an additional 20 min required for cooling simulation. This represents a significant improvement compared to the previous mesh-based numerical model. Table 1 outlines the computational features and simulation performance. Our work expands the model for multi-track simulations despite facing a non-important temperature deviation of 18% confined to the corner of the sintering domain. However, when evaluating the overall temperature level, the error remains below 10% compared to the FEM simulation. Leveraging its high accuracy and speed, the hybrid model is a valuable solution for tackling combinatorial optimization challenges in real-world production settings. This is further elaborated in the rest of the paper.

2. Method

This section first outlines the fundamental governing equations that describe the fluid flow dynamics and thermal behavior during the polymer-based SLS process. Next, a parametric PINN-based PDE solver, and the framework which it rests upon will be introduced. Finally, we detail the simulation domain, parameter setup, and mesh configuration to provide a thorough understanding of the computational aspects of the work.

2.1. Governing physical phenomena and their corresponding equations

2.1.1. Thermal fluid dynamics simulation

This work assumes the flow to be incompressible laminar and the fluid to exhibit Newtonian behavior. Under these assumptions, the PDEs representing the conservation of mass, linear momentum, and energy are utilized to derive the resulting vector and scalar fields.

$$\text{Mass}: \nabla \cdot \mathrm{u} = 0 \tag{1}$$

$$\text{Momentum}: \rho\left[\frac{\partial \mathrm{u}}{\partial t} + (\mathrm{u}\cdot\nabla)\mathrm{u}\right] = -\nabla p + \mu\nabla^2\mathrm{u} - \frac{K_c\left(1-f_{\mathrm{liq}}\right)^2}{C_k + f_{\mathrm{liq}}^3}\mathrm{u} \tag{2}$$

$$\text{Energy}: \rho\left[\frac{\partial h}{\partial t} + (\mathrm{u}\cdot\nabla)h\right] = \nabla\cdot(k\,\nabla T), \tag{3}$$

where $\rho(\mathrm{kgm}^{-3})$ and k $(\mathrm{Wm}^{-1}\mathrm{K}^{-1})$ are density and heat conductivity, respectively. T(K) denotes temperature, $\mathrm{u}(\mathrm{ms}^{-1})$ refers to the velocity field vector, p (Pa) is pressure, and μ (Pa s) stands for viscosity. In Eq. (2), K_c $(\mathrm{kgm}^{-3}\mathrm{s}^{-1})$ and C_k (-) are constants used in the evaluation of the crystallization drag force and, they range from $10^5$to$10^7$and 10^{-5}to10^{-3}, respectively. Additionally, the enthalpy term $h(\mathrm{Jkg}^{-1})$ in Eq. (3) can be expressed as:

$$h = h_{\mathrm{ref}} + c_p\left(T - T_{\mathrm{ref}}\right) + \Delta H f_{\mathrm{liq}}, \tag{4}$$

where c_p $(\mathrm{Jkg}^{-1}\mathrm{K}^{-1})$ is specific heat, $\Delta H(\mathrm{Jkg}^{-1})$ is the latent heat due to crystallization, and $f_{\mathrm{liq}}(-)$ is the fraction of liquid material. The subscript $()_{\mathrm{ref}}$ means the reference state. f_{liq} follows a linear function during crystallizations:

Table 1
Computation time and Capability of different simulation models in single-track simulation for SLS of polymer.

Model type	FVM thermal fluid dynamic model on powder bed [39]	FVM thermal fluid dynamic model on dense substrate	FEM conduction model	Hybrid conduction model
Computation time	3 weeks	4 days	6 h	0.7 s + 20 mins
Capability of model	• Melt pool sizes • Lack of fusion • Porosity • Surface roughness	• Melt pool sizes • Lack of fusion	• Melt pool sizes • Lack of fusion	• Melt pool sizes • Lack of fusion

$$f_{\mathrm{liq}} = \begin{cases} 0 & T < T_{\mathrm{crys}} \\ \dfrac{T - T_{\mathrm{crys}}}{T_{\mathrm{liq}} - T_{\mathrm{crys}}} & T_{\mathrm{crys}} \leq T \leq T_{\mathrm{liq}} \\ 1 & T > T_{\mathrm{liq}}, \end{cases} \tag{5}$$

where T_{crys} and T_{liq} are crystallization and liquidus temperatures. The temperature-dependent thermal physical properties are volume-averaged based on the fraction of liquid and solid, i.e.:

$$\rho = \rho_{\mathrm{crys}} f_{\mathrm{crys}} + \rho_{\mathrm{liq}} f_{\mathrm{liq}} \tag{6}$$

$$C_p = \frac{\rho_{\mathrm{crys}} c_{p,\mathrm{crys}} f_{\mathrm{crys}} + \rho_{\mathrm{liq}} c_{p,\mathrm{liq}} f_{\mathrm{liq}}}{\rho_{\mathrm{crys}} f_{\mathrm{crys}} + \rho_{\mathrm{liq}} f_{\mathrm{liq}}} \tag{7}$$

$$k = k_{\mathrm{crys}} f_{\mathrm{crys}} + k_{\mathrm{liq}} f_{\mathrm{liq}} \tag{8}$$

Concerning thermal boundary conditions of Eq. (3), the part of the top surface which is exposed to the laser will be heated by it, whereas the rest of the top surface will strictly speaking be subject to radiation as well as convection. However, in the present case, the build chamber will be close to vacuum and moreover the particles are preheated to 172 °C, which suggests that radiation and convection can be neglected and replaced by an adiabatic boundary. This was further confirmed by doing simulations where radiation and convection were included, and very little difference was noticed as compared to neglecting them. Consequently, the boundary condition at the top surface can be expressed by the laser power source term as:

$$k\frac{\partial T}{\partial \mathrm{n}} = q''_{\mathrm{laser}} \tag{9}$$

q''_{laser} ($\mathrm{W\ m^{-2}}$) is the surface heat flux due to laser heating and the intensity is assumed to follow the Gaussian distribution, expressed in Eq. (10).

$$q''_{\mathrm{laser}} = \frac{2\alpha p}{\pi r_b^2} \exp\left(-2 \cdot \left(\frac{r}{r_b} \right)^2 \right), \tag{10}$$

where p(W) is the laser power, $\alpha(-)$ is the absorptivity of the material. r(m) stands for the distance from the considered point to the heat source's center, and r_b(m) is the spot radius. Lastly, due to the non-uniform temperature distribution within the melt pool, both the Marangoni effect and capillary effect become significant factors influencing the melt pool's morphology during manufacturing.

$$\tau_{\mathrm{marangoni}} = \frac{d\sigma}{dT}[\nabla T - \mathrm{n}(\nabla T \cdot \mathrm{n})] \tag{11}$$

$$p_{\mathrm{capillary}} = \sigma_0 + \frac{d\sigma}{dT}(T - T_0)\kappa \tag{12}$$

Eq. (15) and Eq. (16) include $\frac{d\sigma}{dT}$ ($\mathrm{Nm^{-1}K^{-1}}$) representing the gradient of surface tension with respect to the temperature, and κ($\mathrm{m^{-1}}$) is the curvature of the free surface. Additionally, σ_0($\mathrm{Nm^{-1}}$) and T_0(K)are the reference surface tension and reference temperature, respectively. The reference values are specifically chosen at the liquidus point. Fig. 3 presents an overview of all these multiphysical phenomena influencing the melt region morphology in polymer-based SLS.

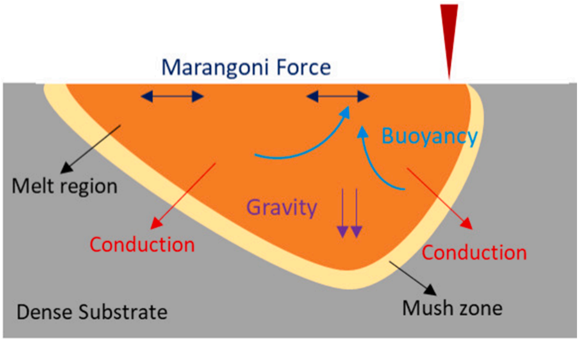

Fig. 3. Schematic of melt region thermal dynamics in polymer-based SLS.

2.1.2. Pure Conduction Simulation

For the pure heat conduction simulation, the contribution from the convective heat transfer is neglected and hence the general energy Eq. (3) is simplified to the transient 3D heat conduction equation, i.e.:

$$\rho c_p \frac{\partial T}{\partial t} = \frac{\partial}{\partial x}\left(k\frac{\partial T}{\partial x}\right) + \frac{\partial}{\partial y}\left(k\frac{\partial T}{\partial y}\right) + \frac{\partial}{\partial z}\left(k\frac{\partial T}{\partial z}\right) - \rho \Delta H \frac{\partial f_{\text{liq}}}{\partial t} + \dot{Q}'' \tag{13}$$

where ρ, c_p, k, and f_{liq} are given by the same expressions specified in the thermal fluid dynamic simulation, i.e. Eqs. (6)–(8). Note that in order to take full advantage of the simplification from CFD to a pure conductive model, we describe the laser heat input with a volumetric heat source accounting for convection effects in a simple way. This typically promotes much faster simulation times as compared to a fully featured CFD model as well as it does not require as fine a surface mesh and small time steps as the surface heat flux would do. The volumetric heat source is given by a Gaussian distribution [36]:

$$\dot{Q}'' = \frac{6\sqrt{3}\alpha p}{\pi\sqrt{\pi} r_b^2} \exp\left(-3\cdot\left(\frac{x-x_0}{r_b}\right)^2\right) \exp\left(-3\cdot\left(\frac{y-y_0}{r_b}\right)^2\right) \exp\left(-3\cdot\left(\frac{z-z_0}{c}\right)^2\right) \tag{14}$$

The coordinates (x_0,y_0,z_0) (m) depict the center of the moving laser source, and c (m) represents the penetration depth of the laser. Other variables, i.e., α, p, r_b, were introduced in the previous section.

2.2. Physics-informed neural network (PINN)

PINN is a type of machine learning model that solves complex physical problems by combining physics-based principles and their associated governing equations with artificial neural networks. In that sense, it leverages neural networks to learn and approximate solutions to the PDEs while adhering to the underlying physics or constraints of the problem. PINNs are typically trained by the governing equations to minimize the overall loss function (or residual), which is expressed as the weighted summation of the loss function for the PDE itself, the loss function for the initial conditions (ICs), and the loss function for the boundary conditions (BCs) when the output function, $\widehat{u}$ is inserted. Note that here we are interested in solving parametric PDEs to study the effect of varying parameters such as laser power, scanning speed, and hatch spacing. Parametric PINNs are particularly suitable for this purpose once they are trained over the range of parameters of interest. For the parametric heat conduction problem in the sintering model, the three loss functions or residuals can be expressed as:

$$\begin{aligned} R_{pde} = {} & \rho c_p \frac{\partial \widehat{u}(t,\mathbf{x};\boldsymbol{\gamma})}{\partial t} - \frac{\partial}{\partial x}\left(k\frac{\partial \widehat{u}(t,\mathbf{x};\boldsymbol{\gamma})}{\partial x}\right) - \frac{\partial}{\partial y}\left(k\frac{\partial \widehat{u}(t,\mathbf{x};\boldsymbol{\gamma})}{\partial y}\right) - \frac{\partial}{\partial z}\left(k\frac{\partial \widehat{u}(t,\mathbf{x};\boldsymbol{\gamma})}{\partial z}\right) \\ & + \rho \Delta H \frac{\partial f_{\text{liq}}}{\partial t} - \dot{Q}'', \mathbf{x} \textbf{ in } \Omega \end{aligned} \tag{15}$$

$$R_{ic} = \widehat{u}(0,\mathrm{x};\gamma) - I(\mathrm{x};\gamma), \ \mathrm{x} \text{ in } \Omega \tag{16}$$

$$R_{bc} = \mathscr{B}(\widehat{u}(t,\mathrm{x};\gamma)) - g(t,x;\gamma), \ \mathrm{x} \text{ in } \partial\Omega \tag{17}$$

where t, x, and γ serve as the input to the PINN. Ω and ∂Ω are computational domain and boundary domain, respectively. Here, t is temporal dimension, x = [x, y, z] are spatial coordinates, and γ = [v, p, h] are laser parameters, i.e., laser speed, laser power, and hatch spacing. In the given equation, $\widehat{u}$ is the output of the neural network as earlier mentioned. In Eq. (16), I(x) refers to the ICs, whereas in Eq. (17), $\mathscr{B}$ and g represent the boundary operators for all BCs. The overall loss or residual of the PINN can hence be formulated as

$$\mathscr{L} = w_{pde}\mathscr{L}_{pde} + w_{ic}\mathscr{L}_{ic} + w_{bc}\mathscr{L}_{bc} \tag{18}$$

$$\mathscr{L}_{pde} = \frac{1}{N_p}\sum_{i=0}^{i=N_p} R_{pde}^2 \tag{19}$$

$$\mathscr{L}_{ic} = \frac{1}{N_i}\sum_{i=0}^{i=N_i} R_{ic}^2 \tag{20}$$

$$\mathscr{L}_{bc} = \frac{1}{N_b}\sum_{i=0}^{i=N_b} R_{bc}^2, \tag{21}$$

where w_{pde}, w_{ic}, and w_{bc} correspond to the weights for each loss term, while N_p, N_i, N_b are the numbers of sampling points in the domain for the respective loss terms. Durning training, the assigned weights of the loss terms will have an impact on learning efficiency. To simplify the corresponding weight tuning, a hard constraint was applied to the initial condition, leading to a reformulation of the network's output as follows:

$$\hat{u}^*(t,\mathrm{x};\gamma) = \hat{u}(t,\mathrm{x};\gamma) \times t + I(\mathrm{x};\gamma), \tag{22}$$

where $\hat{u}^*(t,\mathrm{x};\gamma)$ is the reformulated output ensuring that the initial conditions are always satisfied namely, $\mathscr{L}_{ic} = 0$. Fig. 4 depicts the training scenario of PINN as well as the proposed hybrid framework combining the PINN and FE model. The PINN framework is implemented in the PyTorch package [43] and involved a fully connected neural network with six hidden layers, each comprising of 48 neurons and utilizing the hyperbolic tangent (Tanh) activation function. The optimizer used is Adam [44], with a learning rate set at 2e-5.

2.3. Simulation domain

Regarding the FVM thermal fluid dynamic model, two mesh blocks were employed within the simulation domain, see Fig. 5. The first block uses fine meshing (cell side length of 6 μm) to intricately capture the melt pool dynamics, while the second block employs a coarser meshing (cell side length of 12 μm) to simulate the substrate's thermal impact on the melt pool. In order to reduce the computational cost for single-track simulations, a symmetry boundary condition is applied. A prescribed temperature of 445 K (Dirichlet boundary condition) was applied to the bottom boundary, two boundaries perpendicular to the x-axis, and one boundary perpendicular to the y-axis. This setup effectively simulates the preheating of the powder bed. In the cooling simulation, only a representative 800 μm long section situated in the center is used (as shown in Fig. 5(b)). This focused simulation significantly decreases the computational time for the cooling phase whilst still capturing the overall trend. Consequently, the boundary conditions perpendicular to the x-axis are adjusted to periodic or adiabatic conditions in the cooling step. The material properties are shown in Table 2, and the laser settings are a power of 15 W and a velocity of 3.6 m s^{-1}.

For the thermal conduction simulation, both the FEM-based model and the PINN-based model have the same simulation domain. The laser is activated to begin the sintering process at x = 300 μm and is then deactivated at x = 1800 μm as shown in Fig. 6 (a). Subsequently, the pure conduction cooling simulation continues until the entire domain reaches a temperature lower than the preheating temperature. During both the sintering and cooling phases, the bottom boundary and the boundaries perpendicular to the x-axis and y-axis are subjected to Dirichlet boundary conditions. Fig. 6 (b) shows the mesh settings. The model utilizes mesh refinement

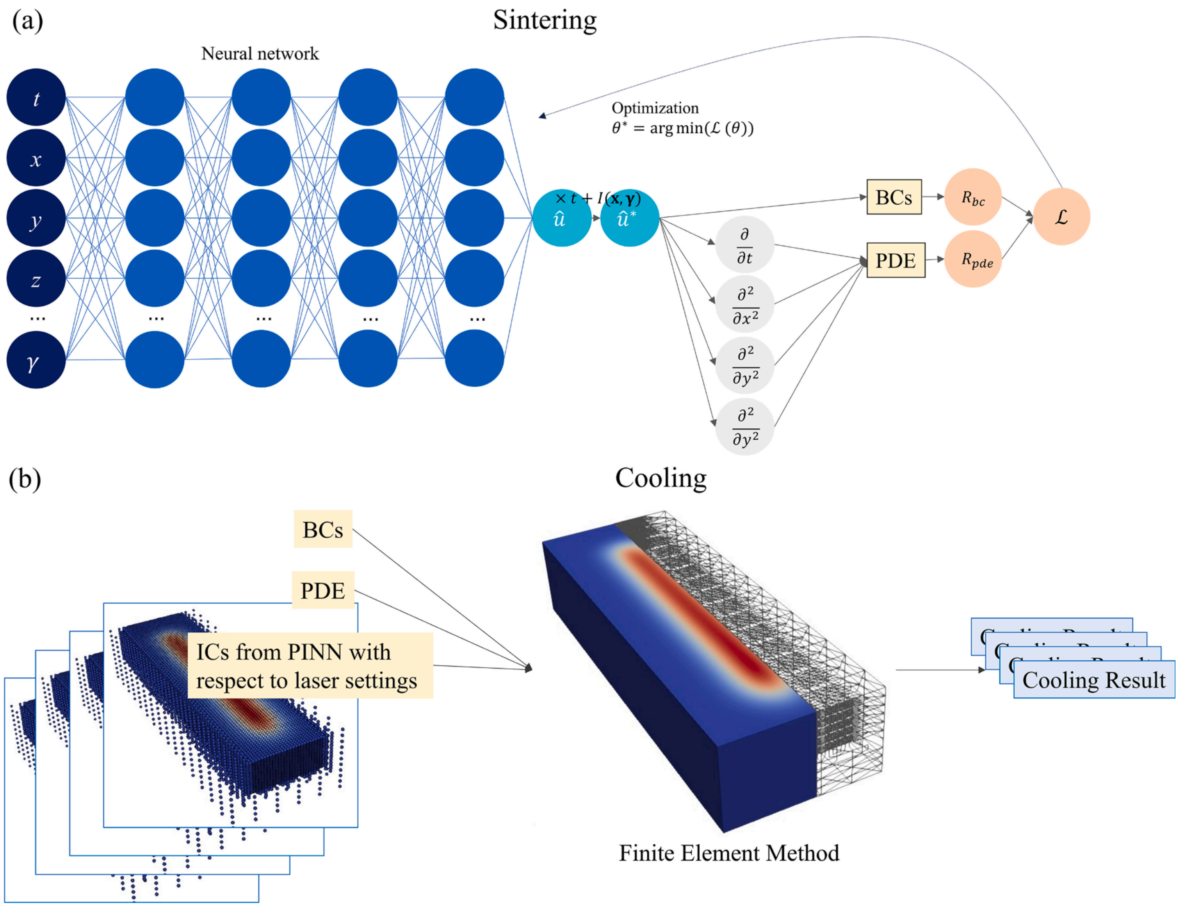

Fig. 4. The overall hybrid model comprised of: (a) parametric PINN sintering model (b) FE cooling model with its initial condition from PINN.

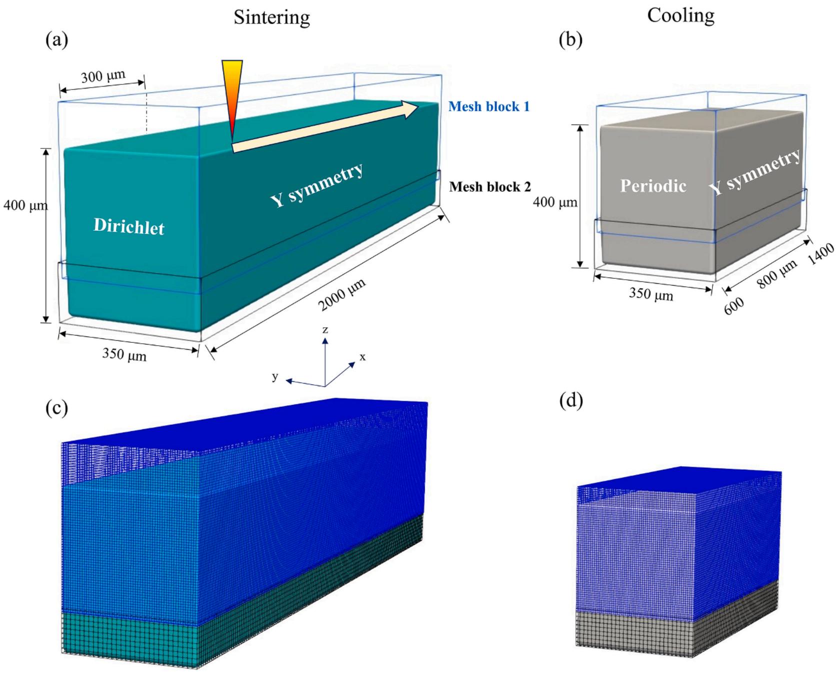

Fig. 5. Single-track simulation domain for the FVM thermal fluid dynamic model (a) During the sintering step (b) During the cooling step (c) Sintering phase mesh configuration (d) Cooling phase mesh configuration.

Table 2
Material properties of PA11 and simulation process conditions.

Property	Value	Property	Value
Density ρ(kgm^{-3})	1030	Viscosity μ (Pas)	250
Conductivity k_s,k_l $(Wm^{-1}K^{-1})$	0.1, 0.3	coefficient of surface tension $\frac{d\sigma}{dT}$ $(\mathrm{N\ m^{-1}K^{-1}})$	-0.065
Specific heat $C_{p,s}$, $C_{p,l}$ (kJkg^{-1}K^{-1})	2.5, 3.0	Reference surface tension σ_0(mNm^{-1})	28.92
Latent heat of melting ΔH(Jkg^{-1})	51870	Material absorptivity α(−)	0.90
Solidus temperature T_{sol} (°C)	184	Laser spot size r_b(µm)	200
Liquidus temperature T_{liq} (°C)	202	Ambient temperature T_{amb}(°C)	172
Laser absorptivity α	0.9		

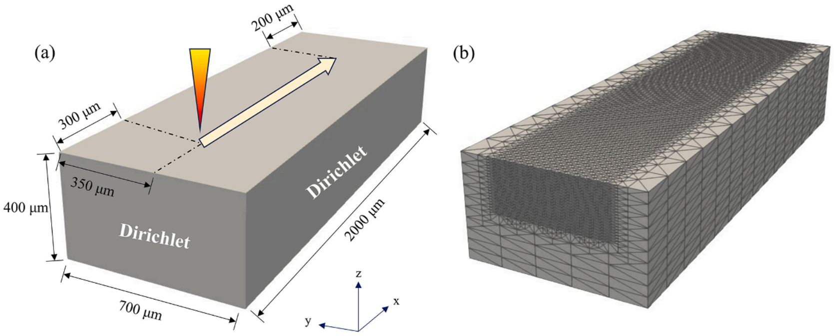

Fig. 6. (a) Heat conduction simulation domain for both FEM and PINN (b) The designed FEM mesh in FEniCS.

specifically near the laser path to enhance computational efficiency. It consists of 82338 elements, featuring an 8 µm characteristic element size near the laser path and larger elements, reaching up to 140 µm, at the outer boundaries of the domain.

The proposed hybrid model uses the simulation domain depicted in Fig. 6 (a). To ensure that the PINN-based sintering part of the hybrid model accommodates various sintering speeds, a total period of 0.6 ms for the simulation was applied. This time frame ensures that the sintering process is completed for different laser speeds within the training interval. Subsequently, after the 0.6 ms duration, the results are transferred to the FEM cooling simulation. Regarding the selection of training points within the domain, 1024 spatial points are randomly chosen, and an extra 300 points are collected spherically centered at the location of the moving heat source with a radius for each temporal point shown in Fig. 7 (a). 512 points are sampled along the boundary where Dirichlet boundary conditions are applied, as shown in Fig. 7 (b). Meanwhile, approximately 64 temporal points are sampled from within the training domain see Fig. 7 (c). The reference for the training interval of laser settings and material properties utilized can be found in Tables 2 and 3.

After this, the hybrid model combining the PINN and FEM models is now applied to multi-track simulation for more realistic printing purposes, and the results are verified using the full FE model (sintering and cooling). The simulation domain is illustrated in Fig. 8. As for the single-track case, the laser performs the sintering process from 300 μm to 1800 μm along the x-direction, moving a hatch distance for each subsequent track until three tracks are completed. Dirichlet boundary conditions are also applied on the four sides and the bottom as before. Comprehensive details of the materials used and laser settings for the simulations are presented in Tables 2 and 3. The meshing procedure in FEM is similar to the single-track simulation. Due to the normalization in the pre-processing applied to the temporal and spatial points in the PINN, a similar sampling procedure could be utilized in the multi-track simulation.

3. Results and discussion

In this section, the validation process begins with the FVM thermal fluid dynamic model applied to a dense substrate and comparing the results with the corresponding data obtained from experiments. Following that, the adequacy of the FE thermal model to describe melt pool morphologies is demonstrated by the small deviation of melt pool sizes when compared with the FVM thermal fluid dynamic model. Finally, the parametric governing equation is solved using the faster and more efficient hybrid model, and its results are verified against those obtained by the FE model.

3.1. FVM thermal fluid dynamic simulation and FEM thermal conduction simulation

Next, the thermal fluid dynamic model is reduced to a pure heat conduction model, and the results are presented in Fig. 9 (b). There is no apparent deviation between cross-sections. Comparing the results from the two simulations in Fig. 10 (a), it is evident that the fully molten region (depicted in dark red) appears somewhat smaller in the thermal fluid dynamic model as compared to the pure conduction model. This variation is attributed to convection cooling, which decreases the melt pool size in the thermal fluid dynamic model. However, the influence of liquid dynamics on the dimensions of the melt region is restrained due to the high viscosity of PA11. Viscosity is even higher in the partially molten region (depicted in yellow and green), further minimizing the fluid dynamics. Consequently, the melt pool dimensions in both the thermal fluid dynamic model and the conduction model exhibit strong similarities as shown in Fig. 10 (b). This is opposed to L-PBF of metals in which the very low viscosity of the molten metal results in considerable convective cooling rendering the predicted melt pool sizes from thermal fluid models and purely conductive models entirely different. Moreover, we conducted a comparison between the heat conduction model with and without air cooling (convection and radiation) in Fig. 10. The results revealed nearly identical melt pool sizes, which can be attributed to the small temperature difference between the ambient environment and the scan line in SLS of polymers, suggesting that air cooling has a limited impact on the melt region and can be disregarded.

The simulation outcomes from both models are validated against experimental results from the literature [39], using a constant laser speed of 3.6 ms^{-1} while varying the laser power between the three values of 10, 12.5 and 15 W, as presented in Table 4 and Fig. 11. The experimental upper limits for weld pool width and depth respectively were obtained by measuring the precise distance between peaks along a single track as shown in Fig. 12. In contrast to this, the lower limits were determined by observing the boundaries between melted and non-melted particles (Fig. 12). Simulation results from both the thermal-fluid as well as the purely conductive

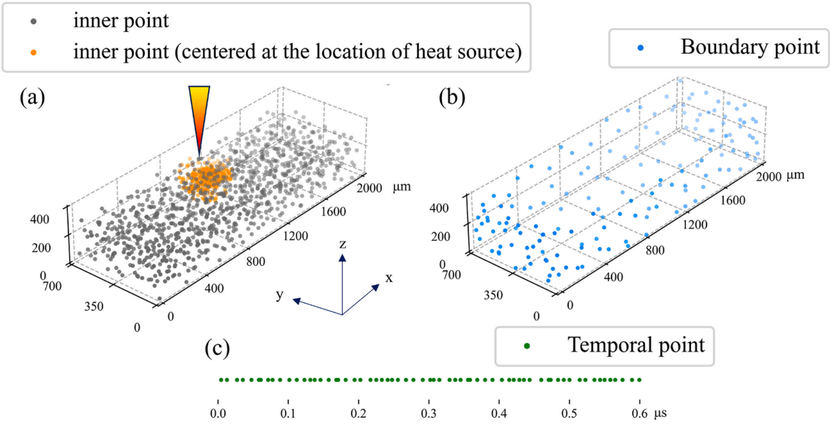

Fig. 7. (a) Sampling points in the spatial domain at time t (b) Sampling points on the spatial boundary (c) Sampling points in the temporal domain.

Table 3
Training set as well as test cases for the hybrid model (PINN/FEM).

Test ID	Laser speed (ms^{-1})	Laser power (W)	Hatch spacing (µm)
Training set	[3.6,4.2, 4.8]	[10,12.5,15]	[120,180,240]
Single-track Test ID			
ST1	4.8	10.0	-
ST2	3.6	15.0	-
ST3	4.0	14.0	-
ST4	3.7	11.0	-
Multi-track Test ID			
MT1	3.7	15.0	130
MT2	4.2	12.0	170
MT3	4.6	11.0	220

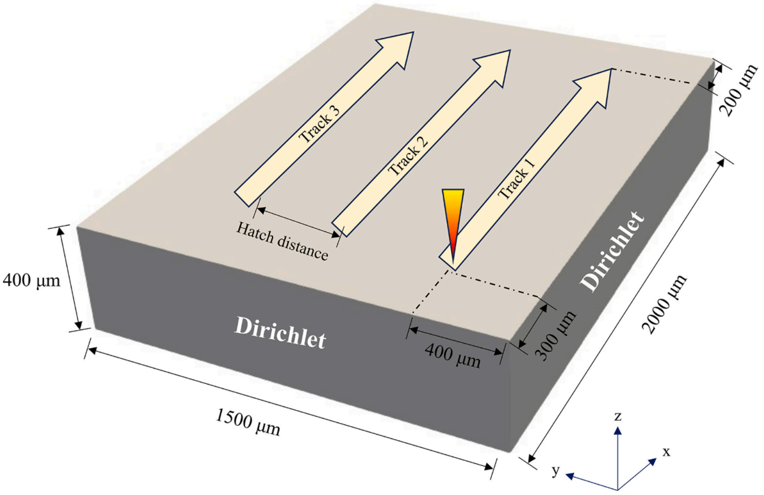

Fig. 8. Multi-track simulation schematic.

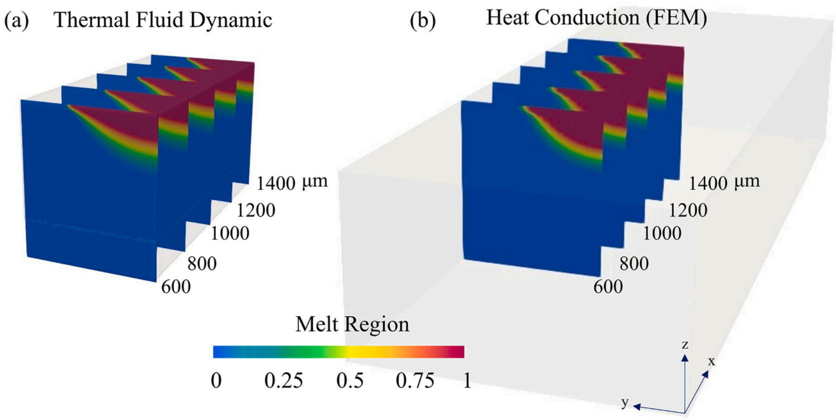

Fig. 9. Cross-sectional analysis on (a) FVM thermal fluid dynamic model (b) FEM thermal conduction model, with laser settings of 15 W and 3.6 m s^{-1}.

model fall within the range of the measurements, indicating that both methods effectively capture the dimensions of the melt region. However, since the thermal-fluid model uses 4 days CPU time whereas the purely conductive model requires only 6 h, and they both predict width and depth within the experimentally obtained limits, the latter is preferred for efficiently simulating the dimensions of the melt region in the SLS of polymers.

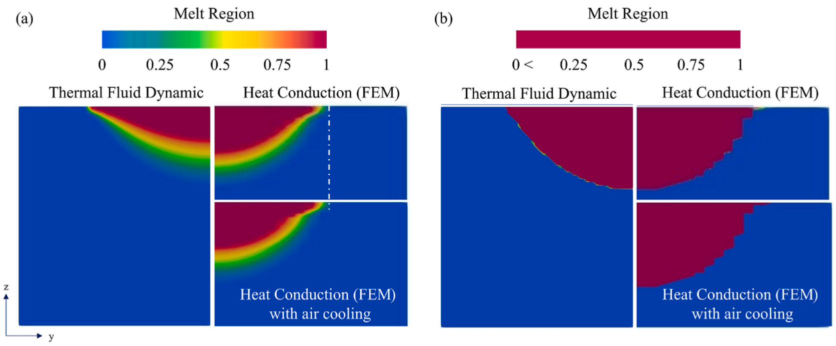

Fig. 10. Cross section of melt region with showing (a) the levels of melting (b) the region of melting level > 0 in FVM thermal fluid dynamic simulation and FEM heat transfer simulation with and without air cooling, with laser settings of 15 W and 3.6 m s^{-1}.

Table 4
Melt region dimensions from experiment [39] and simulations.

Laser Power (W)	10	12.5	15
Melt pool width (μm)			
Measurement lower.	248.82	292.17	384.21
Measurement upper.	373.22	428.84	538.29
FVM Thermal fluid dynamic	–	–	415.56
FEM Thermal conduction	367.12	419.39	424.77
Melt pool depth (μm)			
Measurement lower.	117.01	127.23	149.21
Measurement upper.	209.73	250.84	266.61
FVM Thermal fluid dynamic	–	–	151.67
FEM Thermal conduction	124.12	147.83	168.41

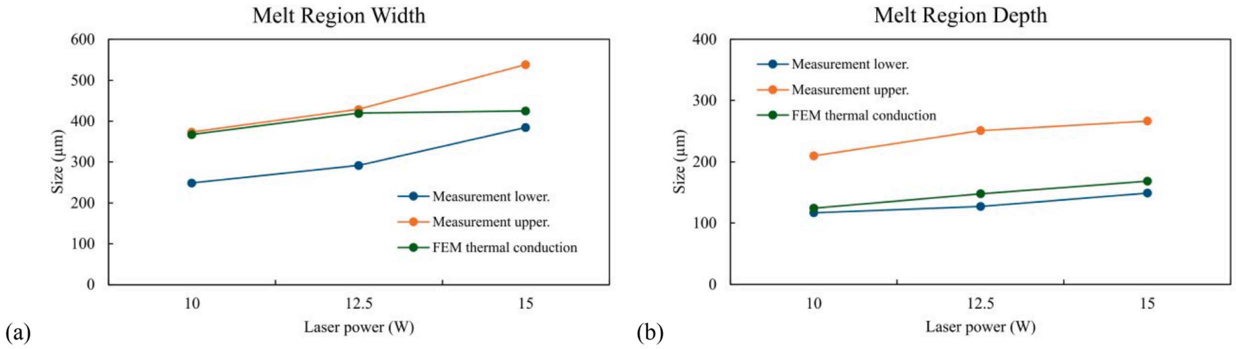

Fig. 11. Melt region (a) width (b) depth with respect to laser power.

3.2. Hybrid PINN and FEM surrogate model

Since the thermal conduction model adequately captures the morphologies of the melt region, it was decided to use this henceforth in the establishment of the hybrid model. More specifically, in the proposed hybrid model, the time-consuming FEM sintering simulation is replaced by a parametric PINN model, while FEM handles the cooling stage. The fidelity of the hybrid model is then verified by comparing its results to the those obtained from the pure conductive FE model.

3.2.1. Single-track result

In the single-track simulation, the input to the parametric PINN consists of a vector including $[t, x, y, z, v, p]$, representing temporal coordinates, spatial coordinates, laser speed, and laser power. The laser speed ranges between 3.6 and 4.8 ms^{-1}, while the laser power varies from 10 to 15 W, following the actual specification in production. Fig. 13 shows the seamless simulation outcomes generated by the hybrid model, illustrating the process from sintering to cooling. The findings also reveal that owing to the notoriously low thermal conductivity, the energy accumulates at the surface during sintering, while eventually transferring downwards as the cooling phase commences. Additionally, for verification purposes, Table 3 outlines the testing scenarios used to assess the accuracy of the parametric model.

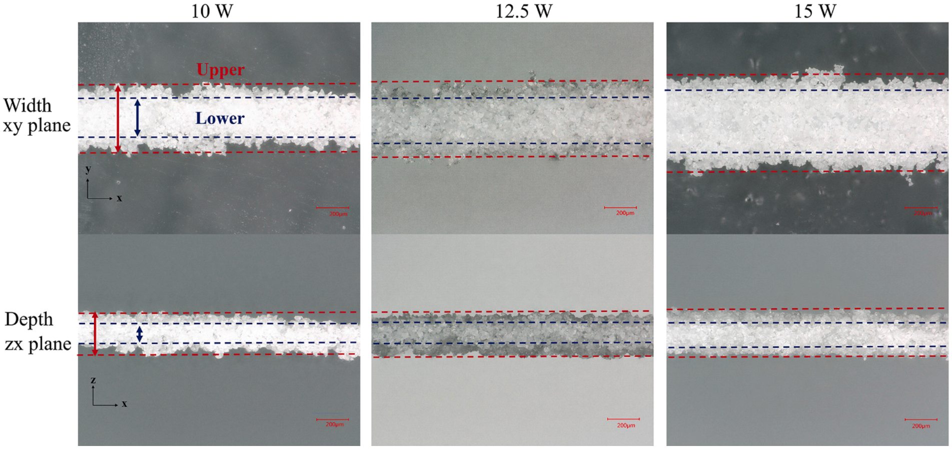

Fig. 12. Single-track experiment result from EOS P110 FDR [39].

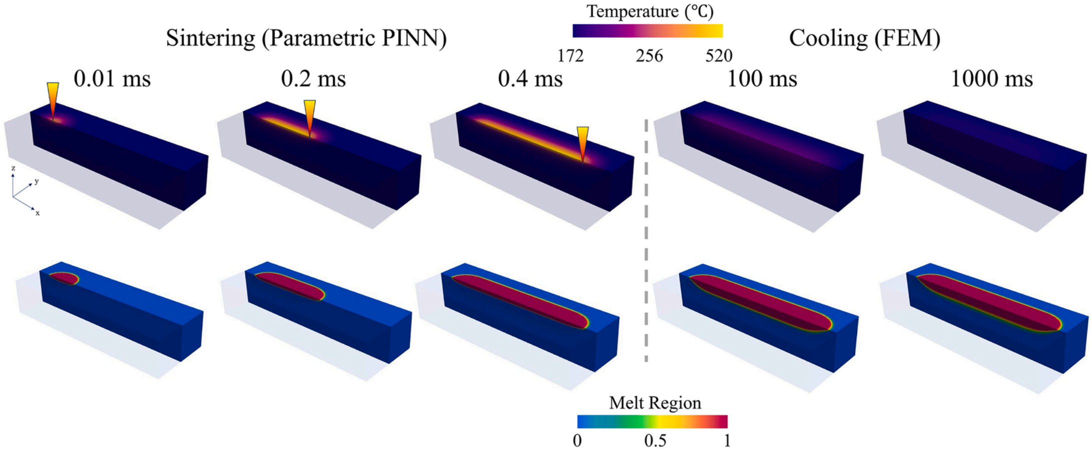

Fig. 13. Simulation result from hybrid model with 3.6 $ms^{-1}$and 15 W laser setting.

Fig. 14 depicts the temperature profiles at the top surface for different instants in time for both models as well as the corresponding percentage deviation between both models at the top surface as well as at the z-x cross-section for y = 350 μm for all the test cases During the sintering phase, the temperature field predicted by the hybrid model matches well with the FEM results, with a maximum percentage error in temperature deviation of 7% across four different test cases. The maximum deviation occurs at the laser starting position once the sintering phase concludes. This might be due to the sampling procedure, as neural networks prioritize training based on points near the moving heat source. As a result, when the heat source reaches the rightmost position, the temperature at the laser's initial point will be too high as compared to the FEM solutions, due to the inherent reduced ability to resolve a high thermal gradient and as well as a high cooling rate.

The simulation results from the parametric PINN serve as initial conditions for the cooling phase in the hybrid model. Given that the solver for the cooling simulation in the hybrid model is also FEM-based, the temperature deviation between this FE model and the full FE model is primarily inherited from the sintering simulation phase. Hence, discussing differences in transient temperature profiles during cooling seems unnecessary. Fig. 15 presents the simulated melt region from the hybrid model and the full FE model, as well as the corresponding deviation. The melt region, defined by the level of liquid fraction, f_{liq}, indicates a fully molten material when $f_{\text{liq}} = 1$. The error map here displays the absolute value of the difference in f_{liq} between the two models. The results show that the melt regions, under the same test settings, exhibit identical width and depth characteristics. Additionally, the deviation indicates a maximum difference of only 0.13 in f_{liq} around the edge of the melt region, which does not significantly affect the overall morphologies of the melt region, where the difference between the results of the two models (width and depth) is actually less than 1%. The entire prediction time, including sintering and cooling, is 0.7 s + 20 mins, using the NVIDIA A100 Tensor Core GPU and Intel Xeon w-2195 processor. Consequently, the suggested hybrid framework, utilizing both PINN and FEM, accurately replicates the sintering and cooling with low computational cost.

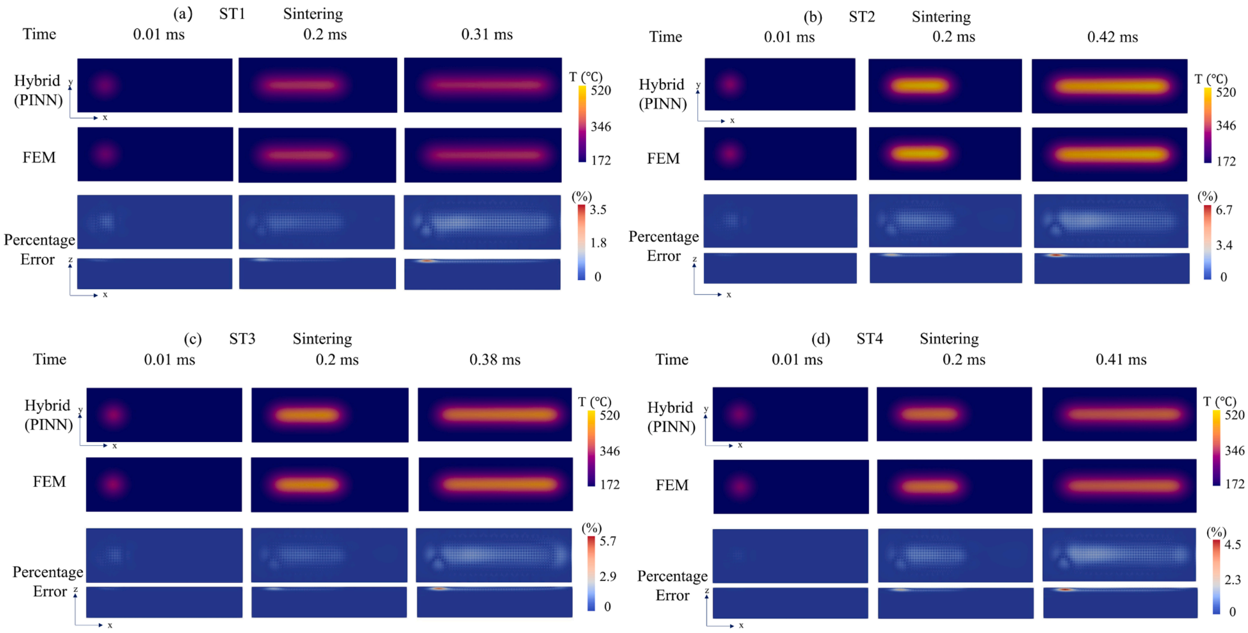

Fig. 14. Surface temperature plots for the single-track simulation from both the hybrid and FEM models. for different instants in time (upper two rows in all four cases). Percentage deviation between the models at the surface (third row in all four cases), and for the z-x cross section at y=350 μm.

3.2.2. *Multi-track result*

The hybrid model addresses the parametric multi-track problem, extending the capabilities beyond single-track simulation. Here, the parametric PINN input resembles the single-track simulation but incorporates an extra variable: the hatch spacing (h), included in the input vector. Specific parameters are defined within realistic ranges based on production specifications: the laser speed varies between 3.6 and 4.8 ms^{-1}, laser power ranges from 10 to 15 W, and hatch spacing spans from 120 to 240 μm. The selected parameter variations are intended to emulate real-world production conditions realistically. Fig. 16 displays the results of the multi-track simulation, providing an overview of both temperature levels and the melt region at the cross section where x = 1000 μm. Similarly as for the single-track simulation, the melt region remains relatively shallow during sintering. Additionally, at 1.25 ms, the depth of the melt region sintered by the first scan line has penetrated further down than for the second and third scan lines. This variation stems from the fact that the temperature propagation perpendicular to the scan line is much slower than the scan speed. Following this, we outline three distinct test cases in Table 3 devised to verify and compare the simulation outcomes obtained from the hybrid model against those calculated from the FE model.

Fig. 17 presents the verification results between the proposed hybrid model and the FEM simulation for the considered multi-track parametric problem. In general, we notice that parametric PINN can calculate the transient temperature field based on the input laser parameters, e.g., speed, power, and hatch spacing. Although there is a maximum percentage error of around 18%, these differences are mainly concentrated around the starting point of each scan line. However, when evaluating the overall temperature level, the errors are under 10% compared to the FEM simulation, indicating a limited influence of peak temperatures and overall profiles. Regarding computer time consumption, the parametric PINN can provide considerable reduction compared to the pure FE simulation, especially in multi-track cases, since the increase in training and inference time is not proportional to the number of tracks and input laser parameters. The training time for the PINN was recorded to 12 h, whereas the actual solution of the heat conduction based on the PINN took just 0.7 s during testing.

In the cooling phase, the hybrid model utilizes FEM as the PDE solver, as earlier mentioned, producing melt regions for the three test cases, as shown in Fig. 18. Comparing the melt regions from the y-z cross-section, the results from both models are in general following the same pattern in all test cases, and the error map further supports this similarity. However, due to the aforementioned differences concentrated especially at the initial point of the scan line, minor deviations in the melt regions are observed from the top view. In general, it can be stated that the hybrid model rapidly and accurately generates temperature profiles and melt region morphologies for both single-track and multi-track cases. Apart from the comparison with the corresponding FEM based results for validation, the temperature fields can also support process analysis and optimization. For instance, in the MT1 simulation presented in Fig. 17 (a), excessive temperature is observed, potentially leading to material degradation. Similarly, Fig. 18 (c) reveals a melt region with uneven edges along the y-axis. In the following section, we will introduce further practical cases concerning process optimization utilizing the hybrid model.

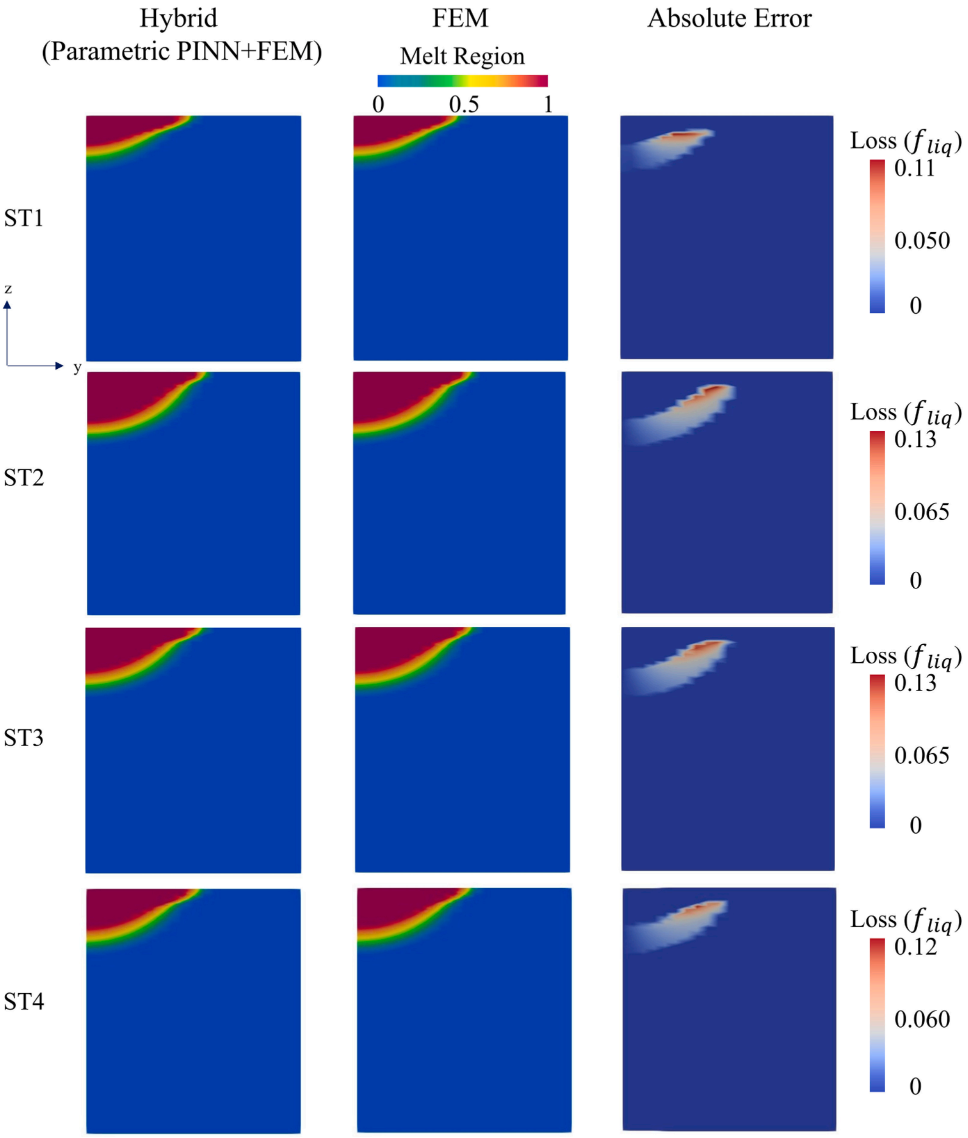

Fig. 15. The melt region for the y-z cross section at x = 1000 µm, for the four test cases as predicted by both the hybrid model and FEM model.

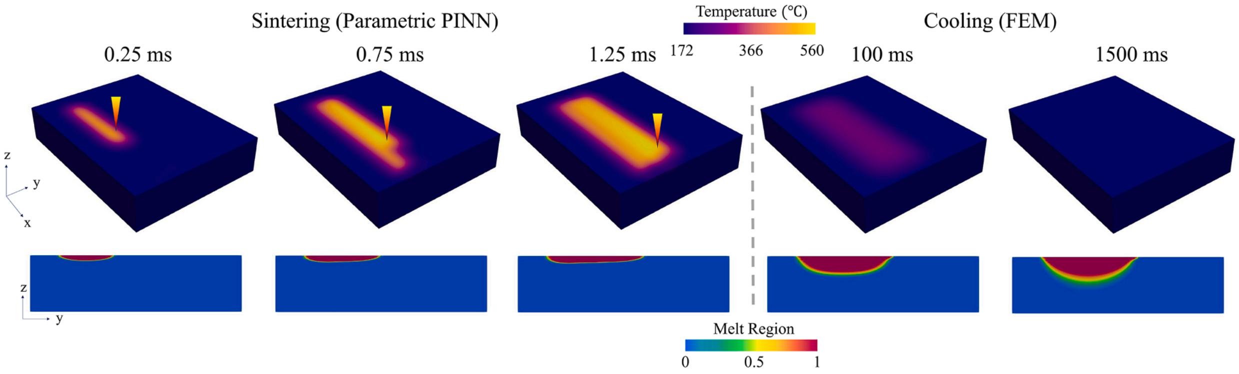

Fig. 16. Multi-track simulation results from the hybrid model with laser speed: 3.6 ms^{-1}, laser power: 14 W, and hatch spacing: 150 µm.

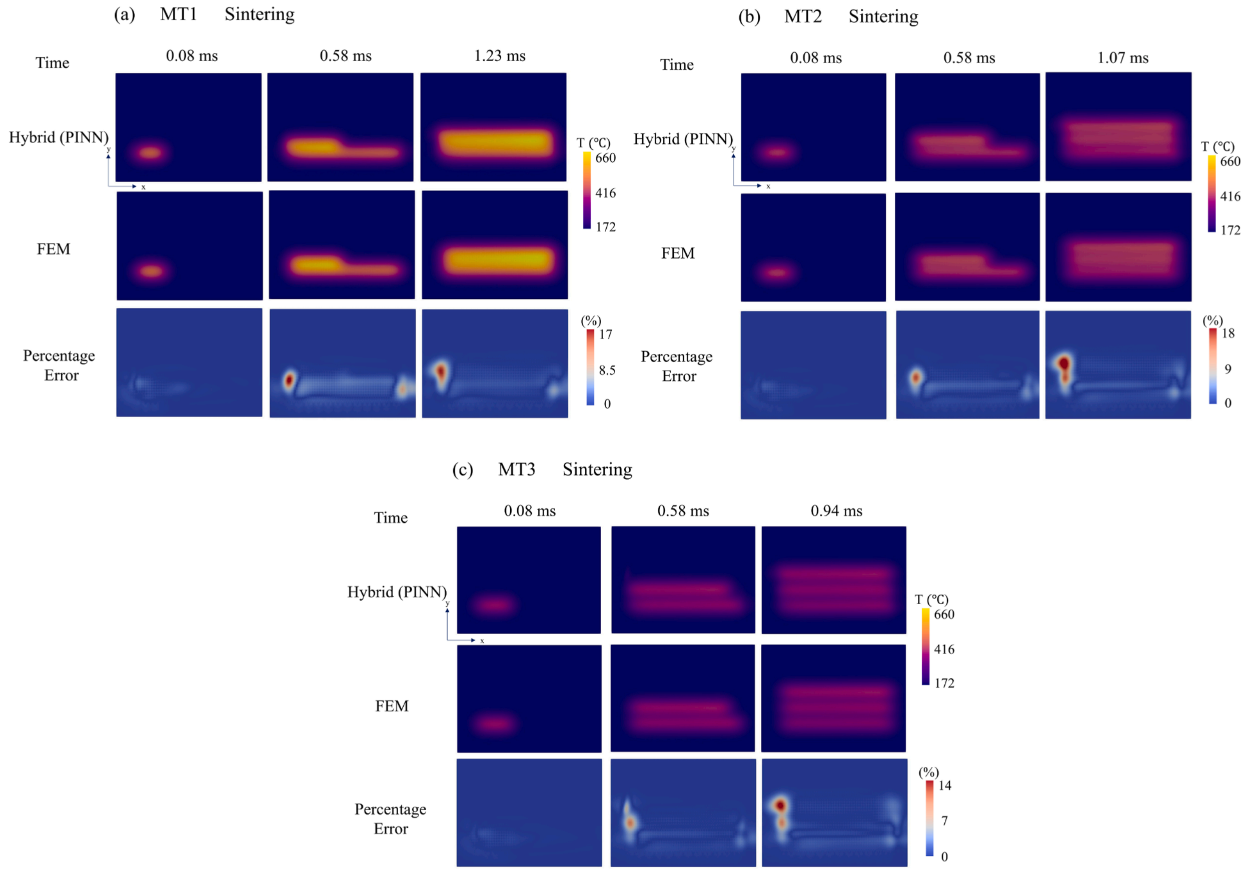

Fig. 17. Comparison of multi-track temperature fields during sintering obtained from both the hybrid and the FEM model at the top surface, along with the percentage error.

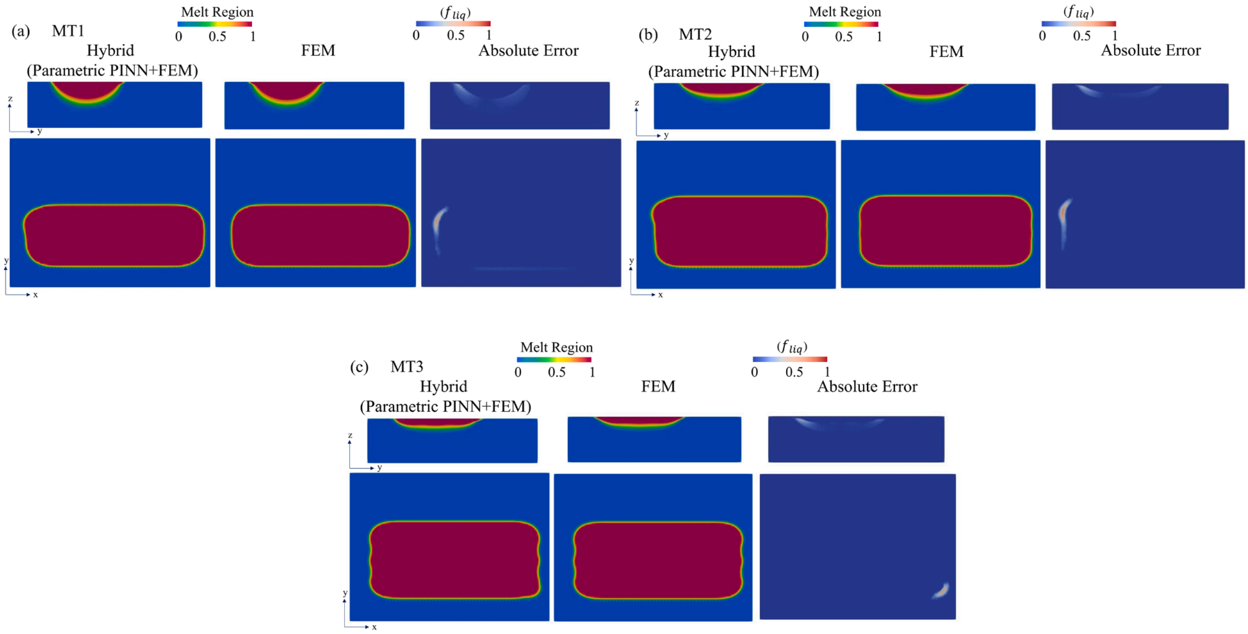

Fig. 18. Melt region from top view (lower row) and y-z cross section at x = 1000 μm (upper row) for the 3 test cases during the cooling after 3 s.

3.2.3. Process parameter selection based on DoE

In polymer-based SLS, achieving optimal hatch spacing, laser speed, and laser power is crucial for ensuring the quality of the final product in a real production line while simultaneously reducing manufacturing time. Using a high-speed laser alongside wider hatch spacing can accommodate this goal. However, such approach may introduce issues like lack of fusion and porosity defects in the final product due to insufficient energy input. In contrast, too much energy leads to high temperatures, potentially leading to material degradation as well as generally reducing the mechanical properties of the material.

In the present work, we use the proposed hybrid model in order to make process parameter selection under two distinct design of experiments (DoEs). In the first DoE shown in Fig. 19 (a), three laser scanning lines are applied sequentially on the domain with varying key process parameters, specifically laser velocity (v), laser power (p), and hatch spacing (h). Our primary objective is to pinpoint optimal configurations that not only prevent material degradation and eliminate lack of fusion but also lead to an efficient manufacturing time per surface area. Moreover, to ensure optimal mechanical properties in the final product, the depth of the melt region must exceed the layer thickness (to ensure sufficient bonding between layers) which in this case is chosen to be 100 μm, representing a commonly used value in industrial application of SLS machines. In other words, if the melt pool depth is below the layer thickness we run the risk of having lack of fusion voids between layers. Moving on to the second DoE, as illustrated in Fig. 19 (b), we outline a five-track sintering process. This process is designed to generate a geometry measuring 1500 μm in length and 600 μm in width. The relevant process parameters in this case include contour laser speed (v_c), hatch laser speed (v_h), and laser power (p) with a fixed hatch spacing of 150 μm. In actual production scenarios, the hatch spacing is often determined by the geometry type and the desired resolution, and the necessity for different scanning speeds at contour and hatch to ensure optimal product quality. Similarly, our aim is to find laser settings that achieve a short manufacturing time without compromising on quality, ensuring a defect-free outcome.

In DoE 1, the process parameters are varied the following way: v (m s^{-1}) = [3.6, 3.9, 4.2, 4.5, 4.8], p (W) = [10, 12.5, 15], and h (μm) = [120, 150, 180, 210, 240]. Because of the manageable number of design variables which is 3 times 25 = 75, a simple brute-force search method is used for exploring the effect of varying the design variables within the parameter space during the sintering phase by analyzing the resulting temperature fields at different instants in time. Subsequently, the final temperature field after sintering for the selected scenarios based on the procedure described below is fed into the simulation of the cooling phase. Fig. 20 (a) depicts the peak temperatures during sintering as predicted by the parametric PINN as a function of the various design variables. Notably, for a fixed laser power, higher speeds, and larger hatch spacings result in lower sintering temperatures, and conversely, lower speeds and smaller hatch spacing lead to higher temperatures. For the PA11 material utilized in this study, thermal degradation occurs at approximately 430°C [45]. Hence, in Fig. 20, "o" represents peak temperatures below that value, whereas "^" indicates peak temperatures above, thus indicating which cases ensure compliance with the constraint to avoid thermal degradation. Next, we only select the scenarios which do not imply degradation for the further cooling simulation in which we do a lack of fusion analysis; see the points marked as "satisfied" in Fig. 20. Analyzing the simulated melt regions derived from the hybrid model, there is no observable lack of fusion defect within the laser settings of DoE 1, see Fig. 21. This supports the fact that the laser settings referenced in this DoE are in line with typical values for this type of SLS machine. Lastly, Fig. 21 displays the melt region as a function of different hatch spacings and laser powers with the highest laser velocity set at 4.8 ms^{-1} for DoE 1. We note that for 10 W and 12.5 W in laser power together with 4.8 ms^{-1}**in** scanning velocity, rough edges marked by orange circles become apparent with increasing hatch spacing. Based on previous works by the authors where we compared simulations and experimental observations, we concluded that a reasonable threshold to determine the size of melt region is $\boldsymbol{f}_{\mathrm{liq}} > 0.5$ [39], and this is also used here to identify the molten region (see the depth indications in Fig. 21). Here, we realize that increasing the hatch spacing to its maximum value of 240 μm, results in melt region depths of 78 μm and 108 μm for laser powers of 10 W and 12.5 W, respectively. Given the hard constraint of surpassing a 100 μm melt region depth and considering the objectives of DoE 1, the settings of 4.8 ms^{-1} laser speed, 12.5 W laser power, and 240 μm hatch spacing will be the

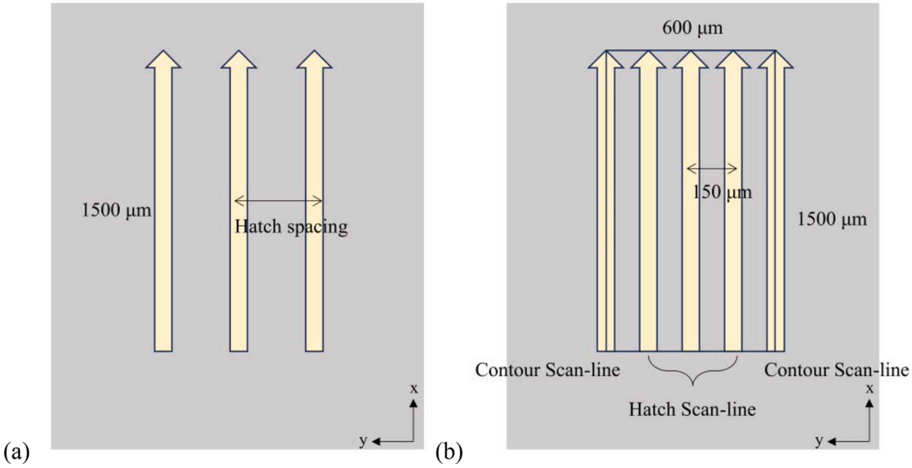

Fig. 19. The top view of domain for process parameters selection (a) DoE 1 (b) DoE 2.

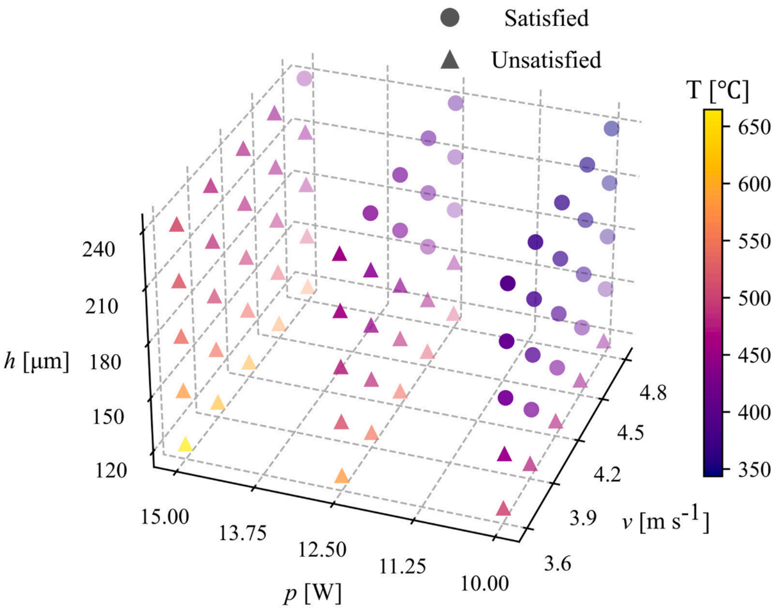

Fig. 20. In DoE, peak temperature predicted by hybrid model during sintering as a function of laser settings ("o" presents lower than degradation threshold, and "^" presents higher than degradation threshold).

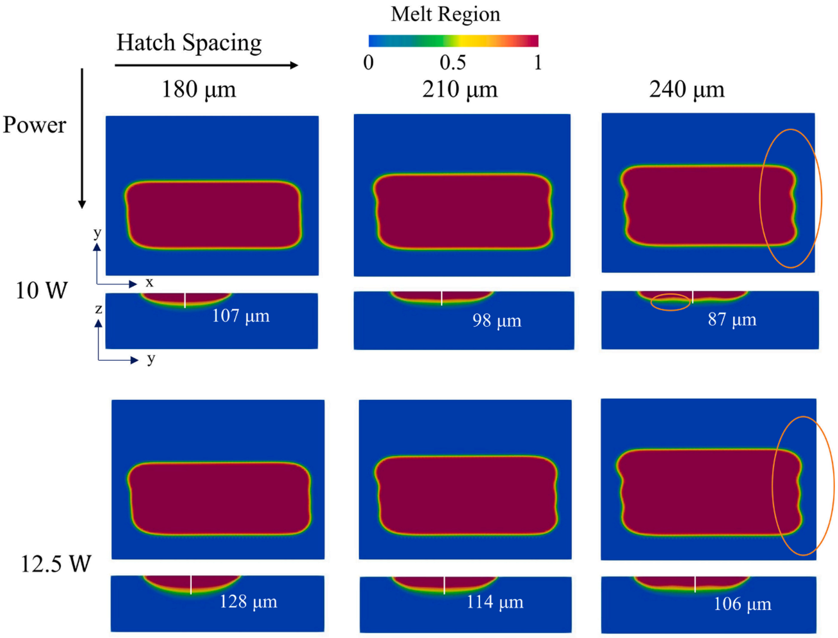

Fig. 21. Melt region of x-y cross section at z= 400 μm and y-z cross section at x=1000 μm by laser speed 4.8 (ms^{-1}) and increased laser power and hatch distance. Cases of rough edges at the end of the scanning tracks as well as wavy penetration depth are indicated by orange ellipses.

optimal ones. It should however be emphasized that even though we do not see any direct lack of fusion in this case, we start observing a wavy behavior of the penetration profile for the case with the lowest laser input per volume, i.e., 4.8 ms^{-1} laser speed, 10 W laser power, and 240 μm hatch spacing, thus indicating a too high hatch spacing for these laser settings.

Within DoE 2, the investigation involves variations in laser power, p (W) = [10, 12.5, 15], the laser speed at the contour, $\boldsymbol{v_c}(\mathbf{ms}^{-1})$ = [3.6, 4.2, 4.8, 5.4, 6], and the laser speed at the hatch, $\boldsymbol{v_h}(\mathbf{ms}^{-1})$ = [3.6, 4.2, 4.8, 5.4, 6], while keeping the hatch spacing constant at 150 μm. Because of the same number of design variables as DoE 1, the brute-force search method is also utilized here. Fig. 22 illustrates the peak temperature during the sintering process, denoting two different symbols to distinguish settings that satisfied or did not satisfy the non-degradation constraint. Also, points marked as satisfied will undergo cooling simulation and lack of fusion analysis.

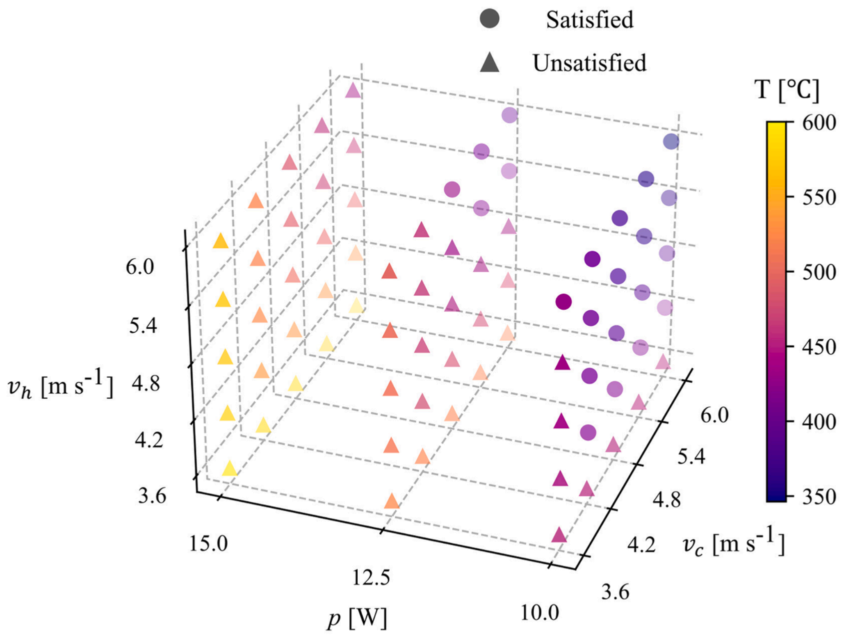

Fig. 22. Within DoE 2, peak temperature predicted by the hybrid model during sintering as a function of laser settings ("o" presents lower than degradation threshold, and "^" presents higher than degradation threshold).

Then, after the cooling simulation and lack of fusion analysis, there is no apparent lack of fusion occurring with the laser settings in DoE 2, either. Hence the laser settings of contour laser speed (v_c) 6 $\mathbf{ms}^{-1}$, and hatch laser speed (v_h) 6 $\mathbf{ms}^{-1}$, will provide the overall fastest sintering process and seem to the preferable combination. However, upon further examination of melt region width and depth within the area where $f_{\text{liq}} > 0.5$ marked by the white boxes in Fig. 23, it is found that this combination does not meet the width requirement of 600 μm for both 12.5 W and 10 W laser power. Consequently, the contour laser speed v_c has to be decreased. Fig. 23 indicates that the laser settings of contour speed (v_c) of 5.4 $\mathbf{ms}^{-1}$and laser power 12.5 W produces a melt region width of 597 μm, aligning closely with nominal width value of 600 μm. Additionally, the melt region depth under these settings reaches 115 μm, which is larger than the powder layer thickness. Therefore, the laser settings of contour laser speed (v_c) 5.4 $\mathbf{ms}^{-1}$, hatch laser speed (v_h) 6 $\mathbf{ms}^{-1}$, and laser power (p) 12.5 W appear to be one of the most suitable. The efficiency of the proposed hybrid model in selecting suitable process parameters under different DoEs and constraints is evident, addressing challenges that are typically difficult for conventional numerical simulations to handle.

4. Conclusion

SLS is an AM technique that uses a laser to build three-dimensional objects by fusing layers of powdered material. While advantageous for producing complex parts, SLS can face defects like lack of fusion, porous structures, and rough surfaces, often due to inadequate melt pool formation from low-power laser settings or excessive energy leading to material degradation. Hence, monitoring the morphologies of the melt region and temperature is crucial for ensuring process stability and product quality. This study introduces a hybrid model combining a parametric physics-informed neural network (PINN) and finite element method (FEM) to simulate polymer-based SLS utilizing PA11 as the material. Motivated by the high computational time for the FVM-based thermal fluid dynamic model on a loose powder bed [39], we specifically present an assessment of the needed computation time for each of the three tested

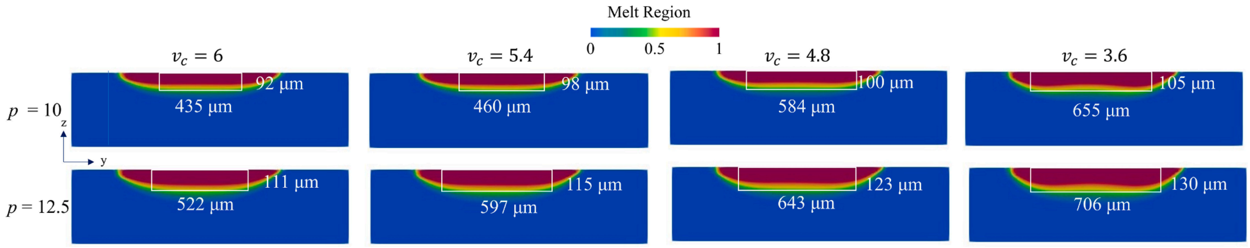

Fig. 23. Melt region of y-z cross-section at x=1000 μm with hatch laser speed 6 ms^{-1}, increasing contour laser speed and 10 W and 12.5 W laser power, respectively.

models (FVM-based thermal fluid dynamic model on dense powder bed, FEM-based heat conduction model, as well as Hybrid PINN and FEM heat conduction model). Specifically, transitioning from the first to the second drastically reduces computational time from 4 days to 6 h. Both models effectively predict both width and depth within the experimentally obtained limits, however the second model requires much less computational time, as stated above. This underscores the effectiveness of the heat conduction model in predicting such morphologies. Subsequently, an AI-powered PDE solver, known for its rapid and parametric capabilities, PINN, is integrated into the hybrid model to simulate the sintering phases and FEM for the cooling phase to predict sintering temperature and melt region morphologies for various laser speeds and velocities, model 3. The model exhibits less than a 7% deviation in temperature and less than 1% in melt pool sizes compared to the FEM-based heat condition model, model 2. With a 7 h training time and significantly reduced prediction time of 0.7 s for sintering and 20 min for cooling, this approach improves computational efficiency over purely mesh-based methods. The study extends the model to perform multi-track simulations despite encountering an 18% error, specifically at the sintering domain corner. Nevertheless, when considering the overall temperature level, the error remains below 10% compared to the FEM simulation. The satisfactory precision and high speed of the hybrid model render it an effective tool for tackling process parameter selection that are typically hard to address using conventional numerical methods in real-world production scenarios.

Declaration of competing interest

The authors have no conflicts of interest to declare.

Data availability

No data was used for the research described in the article.

Acknowledgments

Hao-Ping Yeh was supported by the Manufacturing Academy of Denmark (MADE), specifically through workstream 4, as part of project 05. Amirhossein Arzani acknowledges funding from the National Science Foundation (NSF) Award # 2247173.

References

[1] T.D. Ngo, A. Kashani, G. Imbalzano, K.T.Q. Nguyen, D. Hui, Additive manufacturing (3D printing): a review of materials, methods, applications and challenges, Compos. Part B Eng. 143 (2018) 172–196, https://doi.org/10.1016/j.compositesb.2018.02.012. Elsevier Ltd.

[2] Z.U. Arif, et al., Additive manufacturing of sustainable biomaterials for biomedical applications, Asian J. Pharm. Sci. 18 (3) (2023), https://doi.org/10.1016/j.ajps.2023.100812. Shenyang Pharmaceutical University.

[3] W. Han, L. Kong, M. Xu, Advances in selective laser sintering of polymers, Int. J. Extrem. Manuf. 4 (4) (2022), https://doi.org/10.1088/2631-7990/ac9096. Institute of Physics.

[4] G. Flodberg, H. Pettersson, L. Yang, Pore analysis and mechanical performance of selective laser sintered objects, Addit. Manuf. 24 (2018) 307–315, https://doi.org/10.1016/j.addma.2018.10.001.

[5] M. Bayat, et al., Holistic computational design within additive manufacturing through topology optimization combined with multiphysics multi-scale materials and process modelling, Prog. Mater. Sci. 138 (2023), https://doi.org/10.1016/j.pmatsci.2023.101129. Elsevier Ltd.

[6] A. Das, et al., Current understanding and challenges in high temperature additive manufacturing of engineering thermoplastic polymers, Addit. Manuf. 34 (2020), https://doi.org/10.1016/j.addma.2020.101218. Elsevier B.V.

[7] B.G. Compton, B.K. Post, C.E. Duty, L. Love, V. Kunc, Thermal analysis of additive manufacturing of large-scale thermoplastic polymer composites, Addit. Manuf. 17 (2017) 77–86, https://doi.org/10.1016/j.addma.2017.07.006.

[8] F. Lupone, E. Padovano, F. Casamento, C. Badini, Process phenomena and material properties in selective laser sintering of polymers: a review, Materials 15 (1) (2022), https://doi.org/10.3390/ma15010183. MDPI.

[9] T.G. Spears, S.A. Gold, In-process sensing in selective laser melting (SLM) additive manufacturing, Integr. Mater. Manuf. Innov. 5 (1) (2016) 16–40, https://doi.org/10.1186/s40192-016-0045-4. Springer Science and Business Media Deutschland GmbH.

[10] S. Haeri, Optimisation of blade type spreaders for powder bed preparation in Additive Manufacturing using DEM simulations, Powder Technol. 321 (2017) 94–104, https://doi.org/10.1016/j.powtec.2017.08.011.

[11] V.V. Ganesan, A. Amerinatanzi, A. Jain, Discrete Element Modeling (DEM) simulations of powder bed densification using horizontal compactors in metal additive manufacturing, Powder Technol. 405 (2022), https://doi.org/10.1016/j.powtec.2022.117557.

[12] D. Schiochet Nasato, T. Pöschel, Influence of particle shape in additive manufacturing: discrete element simulations of polyamide 11 and polyamide 12, Addit. Manuf. 36 (2020), https://doi.org/10.1016/j.addma.2020.101421.

[13] Y.S. Lee, W. Zhang, Modeling of heat transfer, fluid flow and solidification microstructure of nickel-base superalloy fabricated by laser powder bed fusion, Addit. Manuf. 12 (2016) 178–188, https://doi.org/10.1016/j.addma.2016.05.003.

[14] M. Bayat, S. Mohanty, J.H. Hattel, Multiphysics modelling of lack-of-fusion voids formation and evolution in IN718 made by multi-track/multi-layer L-PBF, Int. J. Heat Mass Transf. 139 (2019) 95–114, https://doi.org/10.1016/j.ijheatmasstransfer.2019.05.003.

[15] M. Bayat, V.K. Nadimpalli, D.B. Pedersen, J.H. Hattel, A fundamental investigation of thermo-capillarity in laser powder bed fusion of metals and alloys, Int. J. Heat Mass Transf. 166 (2021), https://doi.org/10.1016/j.ijheatmasstransfer.2020.120766.

[16] M. Bayat, et al., Keyhole-induced porosities in Laser-based Powder Bed Fusion (L-PBF) of Ti6Al4V: high-fidelity modelling and experimental validation, Addit. Manuf. 30 (2019), https://doi.org/10.1016/j.addma.2019.100835.

[17] C. Wu, H. Zhao, Y. Li, P. Xie, F. Lin, Surface morphologies of intra-layer printing process in electron beam powder bed fusion: a high-fidelity modeling study with experimental validation, Addit. Manuf. 72 (2023), https://doi.org/10.1016/j.addma.2023.103614.

[18] C. Bierwisch, S. Mohseni-Mofidi, B. Dietemann, M. Grünewald, J. Rudloff, M. Lang, Universal process diagrams for laser sintering of polymers, Mater. Des. 199 (2021), https://doi.org/10.1016/j.matdes.2020.109432.

[19] M. Mollamahmutoglu, O. Yilmaz, Volumetric heat source model for laser-based powder bed fusion process in additive manufacturing, Therm. Sci. Eng. Prog. 25 (2021), https://doi.org/10.1016/j.tsep.2021.101021.

[20] B. Cox, M. Ghayoor, R.P. Doyle, S. Pasebani, J. Gess, Numerical model of heat transfer during laser powder bed fusion of 316L stainless steel, Int. J. Adv. Manuf. Technol. 119 (9–10) (2022) 5715–5725, https://doi.org/10.1007/s00170-021-08352-0.

[21] D. Riedlbauer, M. Drexler, D. Drummer, P. Steinmann, J. Mergheim, Modelling, simulation and experimental validation of heat transfer in selective laser melting of the polymeric material PA12, Comput. Mater. Sci. 93 (2014) 239–248, https://doi.org/10.1016/j.commatsci.2014.06.046.

[22] M.H. Kobir, et al., Prediction of recoater crash in laser powder bed fusion additive manufacturing using graph theory thermomechanical modeling, Prog. Addit. Manuf. 8 (3) (2023) 355–380, https://doi.org/10.1007/s40964-022-00331-5.

[23] J. Wang, Y. Li, R.X. Gao, F. Zhang, Hybrid physics-based and data-driven models for smart manufacturing: modelling, simulation, and explainability, J. Manuf. Syst. 63 (2022) 381–391, https://doi.org/10.1016/j.jmsy.2022.04.004.

[24] A.K. Ball, A. Basak, AI modeling for high-fidelity heat transfer and thermal distortion forecast in metal additive manufacturing, Addit. Manuf. (2023), https://doi.org/10.21203/rs.3.rs-2856513/v1.

[25] M. Roy, O. Wodo, Data-driven modeling of thermal history in additive manufacturing, Addit. Manuf. 32 (2020), https://doi.org/10.1016/j.addma.2019.101017.

[26] Z. Zhang, Z. Liu, D. Wu, Prediction of melt pool temperature in directed energy deposition using machine learning, Addit. Manuf. 37 (2021), https://doi.org/10.1016/j.addma.2020.101692.

[27] K. Ren, Y. Chew, Y.F. Zhang, J.Y.H. Fuh, G.J. Bi, Thermal field prediction for laser scanning paths in laser aided additive manufacturing by physics-based machine learning, Comput. Methods Appl. Mech. Eng. 362 (2020), https://doi.org/10.1016/j.cma.2019.112734.

[28] N. Zobeiry, K.D. Humfeld, A physics-informed machine learning approach for solving heat transfer equation in advanced manufacturing and engineering applications, Eng. Appl. Artif. Intell. 101 (2021), https://doi.org/10.1016/j.engappai.2021.104232.

[29] Q. Zhu, Z. Liu, J. Yan, Machine learning for metal additive manufacturing: predicting temperature and melt pool fluid dynamics using physics-informed neural networks, Comput. Mech. 67 (2) (2021) 619–635, https://doi.org/10.1007/s00466-020-01952-9.

[30] S. Cai, Z. Wang, S. Wang, P. Perdikaris, G.E. Karniadakis, Physics-informed neural networks for heat transfer problems, J. Heat Transf. 143 (6) (2021), https://doi.org/10.1115/1.4050542.

[31] S. Markidis, The old and the new: can physics-informed deep-learning replace traditional linear solvers? Front. Big Data 4 (2021) https://doi.org/10.3389/fdata.2021.669097.

[32] J. Chen, et al., Accelerating thermal simulations in additive manufacturing by training physics-informed neural networks with randomly synthesized data, J. Comput. Inf. Sci. Eng. 24 (1) (2024), https://doi.org/10.1115/1.4062852.

[33] M. Raissi, P. Perdikaris, G.E. Karniadakis, Physics-informed neural networks: a deep learning framework for solving forward and inverse problems involving nonlinear partial differential equations, J. Comput. Phys. 378 (2019) 686–707, https://doi.org/10.1016/j.jcp.2018.10.045.

[34] Y.A. Yucesan, F.A.C. Viana, Physics-informed digital twin for wind turbine main bearing fatigue: quantifying uncertainty in grease degradation, Appl. Soft. Comput. 149 (2023), https://doi.org/10.1016/j.asoc.2023.110921.

[35] M. Aliakbari, M. Mahmoudi, P. Vadasz, A. Arzani, Predicting high-fidelity multiphysics data from low-fidelity fluid flow and transport solvers using physics-informed neural networks, Int. J. Heat Fluid Flow 96 (2022), https://doi.org/10.1016/j.ijheatfluidflow.2022.109002.

[36] E. Hosseini, P. Gh Ghanbari, O. Müller, R. Molinaro, S. Mishra, Single-track thermal analysis of laser powder bed fusion process: parametric solution through physics-informed neural networks, Comput. Methods Appl. Mech. Eng. 410 (2023), https://doi.org/10.1016/j.cma.2023.116019.

[37] S. Li, G. Wang, Y. Di, L. Wang, H. Wang, Q. Zhou, A physics-informed neural network framework to predict 3D temperature field without labeled data in process of laser metal deposition, Eng. Appl. Artif. Intell. 120 (2023), https://doi.org/10.1016/j.engappai.2023.105908.

[38] S. Liao, T. Xue, J. Jeong, S. Webster, K. Ehmann, J. Cao, Hybrid thermal modeling of additive manufacturing processes using physics-informed neural networks for temperature prediction and parameter identification, Comput. Mech. 72 (3) (2023) 499–512, https://doi.org/10.1007/s00466-022-02257-9.

[39] H.P. Yeh, Z. Pan, M. Bayat, and J. H. Hattel, “A Thermal Fluid Dynamic Model for the Melt Region During the Laser Powder Bed Fusion of Polyamide 11 (PA11).” [Online]. Available: https://ssrn.com/abstract=4666120.

[40] W. Yan, et al., Multi-physics modeling of single/multiple-track defect mechanisms in electron beam selective melting, Acta Mater. 134 (2017) 324–333, https://doi.org/10.1016/j.actamat.2017.05.061.

[41] D. Ruggi, M. Lupo, D. Sofia, C. Barrès, D. Barletta, M. Poletto, Flow properties of polymeric powders for selective laser sintering, Powder Technol. 370 (2020) 288–297, https://doi.org/10.1016/j.powtec.2020.05.069.

[42] M.S. Alnaes, et al., The FEniCS project version 1.5, Arch. Numer. Softw. 3 (2015) [Online]. Available: http://fenicsproject.org.

[43] A. Paszke, et al., PyTorch: an imperative style, high-performance deep learning library. Advances in Neural Information Processing Systems 32, Curran Associates, Inc., 2019, pp. 8024–8035 [Online]. Available: http://papers.neurips.cc/paper/9015-pytorch-an-imperative-style-high-performance-deep-learning-library.pdf.

[44] D. P. Kingma and J. Ba, “Adam: a method for stochastic optimization,” CoRR, vol. abs/1412.6980, 2014, [Online]. Available: https://api.semanticscholar.org/CorpusID:6628106.

[45] L. Ferry, R. Sonnier, J.M. Lopez-Cuesta, S. Petigny, C. Bert, Thermal degradation and flammability of polyamide 11 filled with nanoboehmite, J. Therm. Anal. Calorim. 129 (2) (2017) 1029–1037, https://doi.org/10.1007/s10973-017-6244-1.